

Contents lists available at ScienceDirect

Acta Materialia

journal homepage: www.elsevier.com



Full length article

Femtosecond laser rejuvenation of nanocrystalline metals

Glenn H. Balbus^a, McLean P. Echlin^a, Charlette M. Grigorian^b, Timothy J. Rupert^b, Tresa M. Pollock^a Daniel S. Gianola^{a, *}

ARTICLE INFO

Article history:
Received 7 March 2018
Received in revised form 18 June 2018
Accepted 19 June 2018
Available online xxx

Keywords: Nanocrystalline Femtosecond lasers Grain boundaries Rejuvenation

ABSTRACT

Nanocrystalline metals are distinct from traditional engineering materials due to their high concentration of grain boundaries and corresponding structural disorder at grain boundaries. The effect of local disorder in nanocrystalline materials manifests in ways reminiscent of fully amorphous materials, such as mesoscale shear localization and pressure-dependent yielding, owing to the high concentration of grain boundaries and their predominance in governing plasticity. Relaxation processes in nanocrystalline materials that facilitate reconfigurations of grain boundaries and lower their energy, such as low temperature annealing, have been shown to enhance mechanical strength. However, processes that raise the energy of a nanocrystalline metal have not been observed, limiting the tunability of properties and the prospect for suppressing shear localization. Here, we use femtosecond laser processing as a unique non-equilibrium process that can generate complex stress states due to ultrafast electronic excitation and subsequent relaxation events. Experiments on nanocrystalline Al-O and Cu-Zr alloys indicate that sub-ablation femtosecond laser pulses cause up to an 87% reduction in hardness accompanied by negligible changes in grain size, which can be ascribed to grain boundary-mediated processes. Parallels between our results and rejuvenation processes in glassy systems will be discussed in the context of controlling metastable structural configurations through novel processing routes.

© 2018.

1. Introduction

Nanocrystalline (NC) metals have attracted widespread interest due to their desirable mechanical properties, primarily their high strength [1-5] and wear resistance [6]. The mechanical behavior and deformation physics of metals with grain sizes finer than 50 nm are drastically different from their coarse-grained counterparts, due to their inability to facilitate traditional dislocation activity, as well as a high concentration of grain boundary (GB) regions that participate strongly in plastic deformation [4,5,7]. Many of the numerous deformation mechanisms operative in NC metals, for instance, GB sliding [8,9] and dislocation-GB processes (nucleation, propagation, absorption) [10,11], hinge on the local atomic configuration of GB regions. GBs can exhibit a large diversity of both equilibrium and non-equilibrium structures, which can drastically affect the local properties [2,12-14]. The effects of metastable GB configurations on GB energy can be large, and their role in mechanical deformation is expected to be concomitantly so [13-15]. Additionally, imperfections at GBs such as steps, kinks, and ledges can alter their deformation behavior - acting as stress concentrations, mediating the nucleation and propagation of partial dislocations [10]. Other unique deformation

behavior of NC metals, such as stress-assisted grain growth, can be ex-

"top-down" approaches of grain refinement such as high pressure torsion [18] and ECAP [19], as well as "bottom-up" methods such as inert gas condensation [20], electrodeposition [21], and sputter deposition [22], are far-from-equilibrium processes that can produce non-equilibrium, high-energy GB structures [23]. Experimental observations and atomistic simulations of low temperature annealing [3,24,25] and mechanical cycling with amplitudes well below the global yield stress [25] of NC metals show that GB relaxation can dramatically increase the yield strength of these materials without influencing grain size. This behavior has not only been ascribed to GB solute segregation in binary or multicomponent alloys [3,26], but has also been shown to be caused by configurational relaxation in GB regions for both alloy and nominally pure systems [25]. Segregation of solute to GBs serves to decrease the GB energy in systems with a high enthalpy of segregation [3,26] and configurational relaxation of non-equilibrium GB structures also reduce the energy of these systems [25], increasing the activation barrier to initiate plasticity. This sensitivity to local chemistry and structure, coupled with molecular-dynamics simulations indicating a multiplicity of metastable GB

Email address: gianola@ucsb.edu (D.S. Gianola)

^a Materials Department, University California, Santa Barbara, CA 93106, USA

^b Chemical Engineering and Materials Science, University of California, Irvine, CA 92697, USA

plained by the evolution of GB structures during plastic deformation [16,17]. These results collectively underscore the notion that the local atomic structure at GBs plays a crucial role during the deformation of NC metals.

Processing routes utilized to synthesize NC metals, including

^{*} Corresponding author.

states for a macroscopically fixed GB [14,15], suggests that far-from-equilibrium processing routes like those used to produce NC metals may enable the formation of metastable GB structures underpinning their thermomechanical response. Chemical and structural effects may also occur in concert, wherein solute segregation to GBs has been shown to drive structural transformations at the GB [27].

Sensitivity to thermomechanical history and abundant structural disorder in interface dominated materials like NC metals, suggested by a multiplicity of metastable configurations of GBs, is reminiscent of fully amorphous materials, such as metallic glasses (MGs), which are often described as the limit of grain refinement [28]. Several researchers have noted similarities between the mechanical behavior of these materials [29–32], such as pressure dependent yielding [29] and strong shear localization [32]. Others have shown kinetic similarities between GB regions in coarse grained materials and MGs [33]. Due to the predominance for GB-mediated plasticity in NC metals, applying the understanding of MG deformation to GBs in NC metals may enable enhanced control over the mechanical behavior of NC metals.

Despite the numerous similarities between these two materials, commonalities in the history and processing dependence between NC metals and MGs have received little attention. MGs show a strong history dependence, where a more relaxed - i.e. a lower energy atomic configuration – glass has a higher yield strength and propensity for shear localization [34]; whereas a more rejuvenated – i.e. higher in energy, more liquid-like – glass has increased ductility [35]. Processing routes used to modify the energy of a MG to exploit tunable properties have been studied extensively, notably to facilitate homogeneous plasticity at room temperature [35-38]. Relaxation processing routes are similar to those for NC metals – low temperature annealing $\lceil 34 \rceil$ and cyclic mechanical loading [39] both produce increases in yield stress and modulus of a MG. Conversely, rejuvenation processes include severe plastic deformation [40], and cryogenic cycling [41], which induce local dilatational strains, decreasing the yield strength and modulus, but increasing the ductility of the MG. Rejuvenation of an MG can be correlated to increases in free volume, stored enthalpy, and fictive temperature, but can be defined as an increase in energy of system [35-38,40-42].

Rejuvenation processing has enabled greater functionality of MGs by enhancing their ductility, allowing for stable plastic deformation at room temperature. NC metals exhibit similar mechanical instabilities that limit their use, thus the potential of rejuvenation processing routes to enhance their properties is tantalizing. To date, no single processing route, or combination thereof, has been identified that can bi-directionally tailor the state of GBs, despite these strategies being recently employed for MGs. These processing routes categorically occur quickly and at low temperature, in order to suppress any competing structural relaxation [42]. A previously unexplored processing technique that possesses these characteristics is pulsed ultrafast laser processing. Unlike longer pulse laser-material interaction, which have been used as heat sources for processing of both NC metals and MGs [43–45], femtosecond (fs) pulse laser-material interactions are fundamentally different, due to the difference in timescales between

electronic excitation (fs) and phonon-electron relaxation (ps) [46]. This difference in timescales facilitates a largely athermal, mechanical ablation process, which is useful in mitigating damaged zones during machining [47]. High fluence fs-laser processing has been used extensively for micromachining, enabling serial sectioning and micromechanical sample preparation, as well as other applications where material removal with minimal residual damage is required [48,49]. Many experimental observations and computer simulations have studied the ablation behavior of materials exposed to high fluence fs-laser irradiation [47,50-56]. Recent work has indicated that grain size affects fs-laser ablation, because fs-laser-material interactions at GB regions are fundamentally different than in bulk crystalline regions due to spatially heterogeneous electron-phonon coupling behavior [55]. While the bulk of the investigation into fs-laser-matter interactions have been focused on high fluence ablation behavior, hybrid two-temperature model/molecular-dynamics simulations have indicated that at energies below the ablation threshold, significant tensile and compressive stresses can be induced by the laser [55,56]. The resulting combination of high stresses, short timescales, largely athermal processing, and potential confinement to GB regions suggests that the fs-laser processing may have the characteristics necessary for rejuvenation of GBs, analogous to processing developed by the MG community.

We hypothesize that the stresses generated by the fs-laser at energies below the ablation threshold may be used to modify the mechanical behavior of NC metals via short-range atomic rearrangements at GBs, where when incurred due to thermal and mechanical cycling have been shown to cause dramatic shifts in mechanical properties with negligible microstructural evolution. In this work, we report on measurements demonstrating the influence of sub-ablation threshold femtosecond laser pulses on location-specific properties of NC Al-O and Cu-Zr, materials selected to explore a range of different GB chemical and structural states. Our results suggest that sub-ablation femtosecond laser pulses cause a dramatic and recoverable reduction in hardness accompanied by negligible changes in grain size, reminiscent of rejuvenation processes in MGs.

2. Materials and methods

NC Al-O samples were synthesized by magnetron co-sputtering of 99.999% pure Al and 99.995% pure α -Al₂O₃ in an Explorer 14 Sputtering system (Denton Vacuum) on Si (100) wafers and Cu transmission electron microscopy (TEM) grids with C support films at DC powers of 200–300W for the Al target and RF powers of 0–150W for the α -Al₂O₃. These deposition parameters resulted in compositions of Al-0.82±0.10 at.%O and Al-4.79±0.48 at.%O. From here on, the samples will be referred to as Al-0.8 at.%O and Al-4.8 at.%O. Additional details of the NC Al-O sample preparation are located in Ref. [22]. Compositional information, film thickness, grain size and initial hardness information are shown in Table 1. Bright field (BF) TEM images of both as-deposited NC Al samples are shown in Fig. 1 (a, b).

Table 1
Summary of samples utilized in this work – chemistry, average grain size, and optical parameters obtained from literature, as well as non-irradiated indentation hardness and ablation thresholds

Material	tfilm (nm)	Csolute (at. %)	d (nm)	H ₀ (GPa)	Ablation Threshold (J cm ⁻²)	Optical Absorption Coefficient κ	Optical Penetration Depth δ (nm)
Al-0.8 at.%O	156	0.8 ± 0.1	84	1.5 ± 0.3	0.20 ± 0.02	8.46	7.3
Al-4.8 at.%O	210	4.8 ± 0.5	19	2.3 ± 0.7	0.15 ± 0.02	8.46	7.3
Q-Cu-Zr	*	3 ± 0.1	42	3.0 ± 0.6	0.33 ± 0.02	4.82	13
SC-Cu-Zr	*	3 ± 0.1	43	3.0 ± 0.7	0.50 ± 0.02	4.82	13

^{*}Q-Cu-Zr and SC-Cu-Zr are powder samples prepared by ball milling

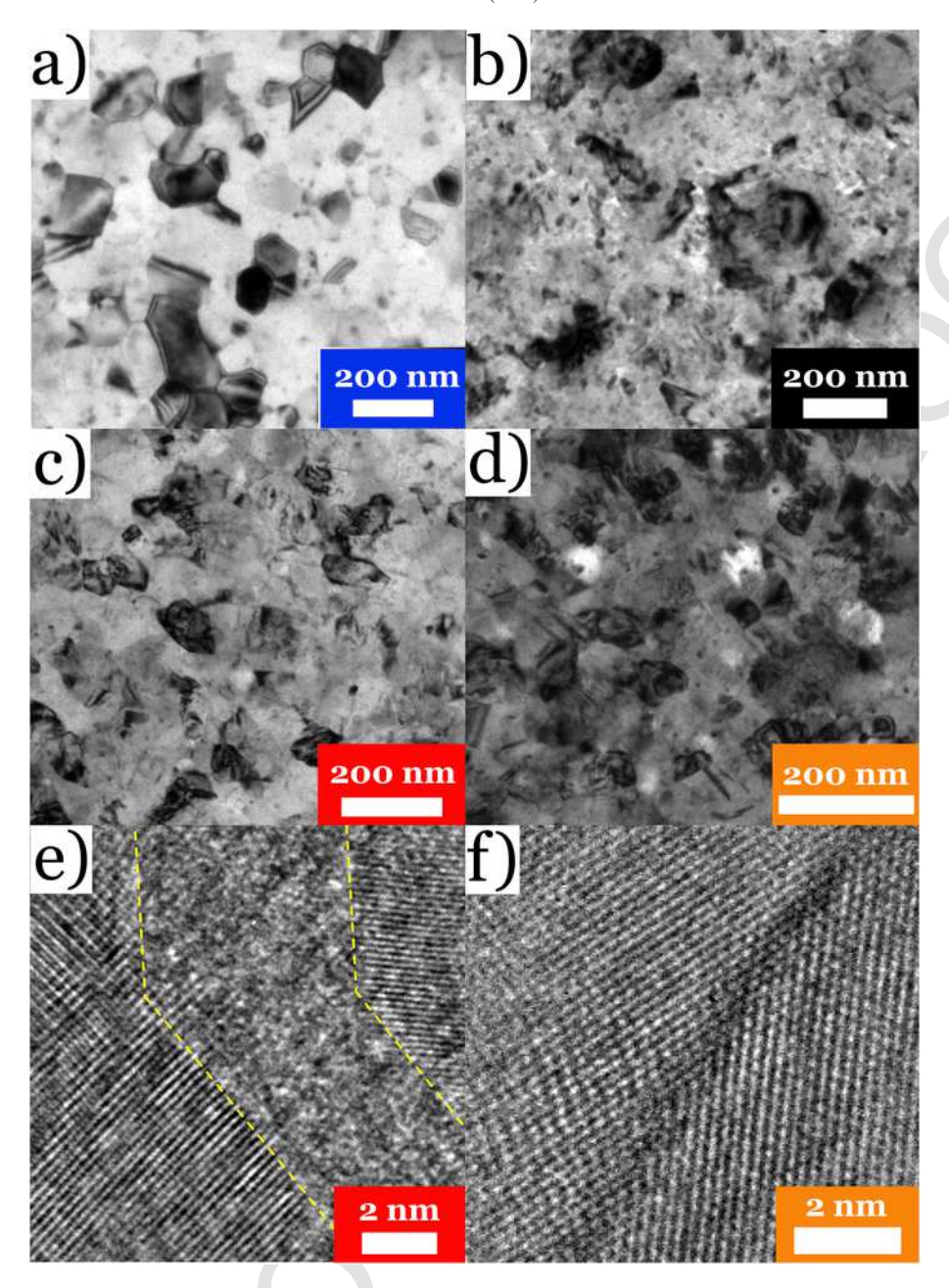


Fig. 1. TEM images of all samples utilized in this study. a) BF image of Al-0.8 at.%O sample. Corresponding data plotted in blue. b) BF image of Al-4.8 at.%O sample. Corresponding data plotted in black. c) BF TEM image of Q-Cu-Zr, corresponding data plotted in red. d) BF TEM image of SC-Cu-Zr, corresponding data plotted in orange. e) HRTEM image of Q-Cu-Zr, amorphous region indicated by dashed yellow lines. f) HRTEM image of SC-Cu-Zr. No amorphous region is present at the GB shown. (For interpretation of the references to colour in this figure legend, the reader is referred to the Web version of this article.)

NC Cu-3 at.%Zr samples were prepared using mechanical ball milling in a SPEX SamplePrep 8000 M Mixer/Mill to produce powders with µm-sized particle diameters and nm-sized grains. Powders were milled for 10 h using a hardened steel vial and milling media, and stearic acid in the amount of 2 wt% was added as a process control agent. Annealing treatments were performed at 950 °C in vacuum for 1 h to promote Zr diffusion to GBs and allow for the formation of amorphous intergranular films (AIFs). Samples were then either rapidly quenched in water or slowly cooled in air from the annealed state. TEM specimens of both quenched and slowly cooled samples were made using a FEI Quanta 3D FEG scanning electron microscope (SEM) equipped with a focused ion beam (FIB), with a final

5 kV polish to remove excess FIB damage. Specimens were inspected using a FEI Titan TEM operating at 300 kV in order to investigate the microstructure and GB structures at each annealing condition. Rapidly quenching stabilized the microstructure at high temperature, including any AIFs present at GBs. BF and high resolution TEM (HRTEM) images of this sample are shown in Fig. 1 (c, e), where the presence of this amorphous region is demonstrated by the mottled region outlined in the image. It is important to note that AIFs are not found at every GB throughout the microstructure, and a variety of complexion types and thicknesses are commonly found within a given sample. In Ref. [57], AIFs as thin as 0.5 nm and as thick as

5.7 nm were observed in a quenched Cu-Zr sample; however, sharp GBs were also present within the same sample.

Slowly cooling the samples resulted in sharp GBs, as shown in the BF and HRTEM images in Fig. 1d. No AIFs were observed in the slowly cooled sample, as the glassy Cu-Zr phase which exists in equilibrium at GBs at the annealing temperature cannot exist in equilibrium at room temperature. While the boundary structure is very different in these two samples, both have interfaces that are decorated with Zr due to the GB-segregation process. Due to the exceptional thermal stability of these samples [57,58], the high annealing temperatures during sample preparation do not cause grain growth, and both samples have similar initial grain sizes. These two samples will henceforth be referred to as Q-Cu-Zr (quenched) and SC-Cu-Zr (slowly cooled). Additional details are available in Ref. [57]. Compositional information, grain size, and initial non-irradiated hardness information are located in Table 1.

Laser treatments were performed using a Clark MXR CPA-2110 Series Ti:Sapphire Ultrashort Pulse Laser with a 1 kHz repetition rate, 780 nm wavelength, and 150 fs pulse width in air (22 °C, 42–70% relative humidity). The output power variability of the laser was less than 1%. The beam was attenuated with a series of neutral density filters and a rotating half-wave plate followed by a p-polarized beam splitter before being focused down by a 500 mm focal length plano-convex lens with a $1/e^2$ radius of $30.8\,\mu m$ measured as described in Ref. [59]. Average laser energies were measured using an Ophir Photonics High Sensitivity Thermal Laser Sensor. All experiments were

conducted with an average power in the range of 0-15 mJ, corresponding to fluences of 0-0.5 J cm⁻². Ablation thresholds were characterized by performing a series of non-overlapping single pulse arrays at fluences between 0.037 J cm⁻² and 0.3 J cm⁻² in increments of 0.015 J cm⁻². The onset of ablation was determined by measuring changes in sample height across the irradiated regions using an Asylum MFP-3D atomic force microscope in tapping mode, following the procedure in Ref. [60]. These values and corresponding errors are presented in Table 1. To collect sufficient information for subsequent nanomechanical evaluation, areas of $\sim 0.01 \,\mathrm{mm}^2$ were irradiated with single pulses by translating the stage 10 µm between subsequent laser pulses, as illustrated in Fig. 2a. Fig. 2b shows an area that was irradiated with a fluence above the ablation threshold, which is included to demonstrate the process. Fig. 2c shows an area treated with a fluence below the ablation threshold with no obvious changes to the surface. The fluences reported are the average single pulse fluences measured prior to treatment. Due to the slight overlapping pulse geometry. the reported number of pulses is a lower bound on the effective pulse count experienced by the sample.

To measure the effects of fs-laser treatments on the mechanical properties of these materials, nanoindentation experiments were performed using a Nanomechanics iMicro[®] Nanoindenter equipped with a 50 mN load cell. Hardness measurements were performed with a Berkovich tip diamond indenter. All hardness measurements were performed at an indentation strain rate of 0.2 s⁻¹. The tip area function of the Berkovich tip was calibrated on fused silica before and af-

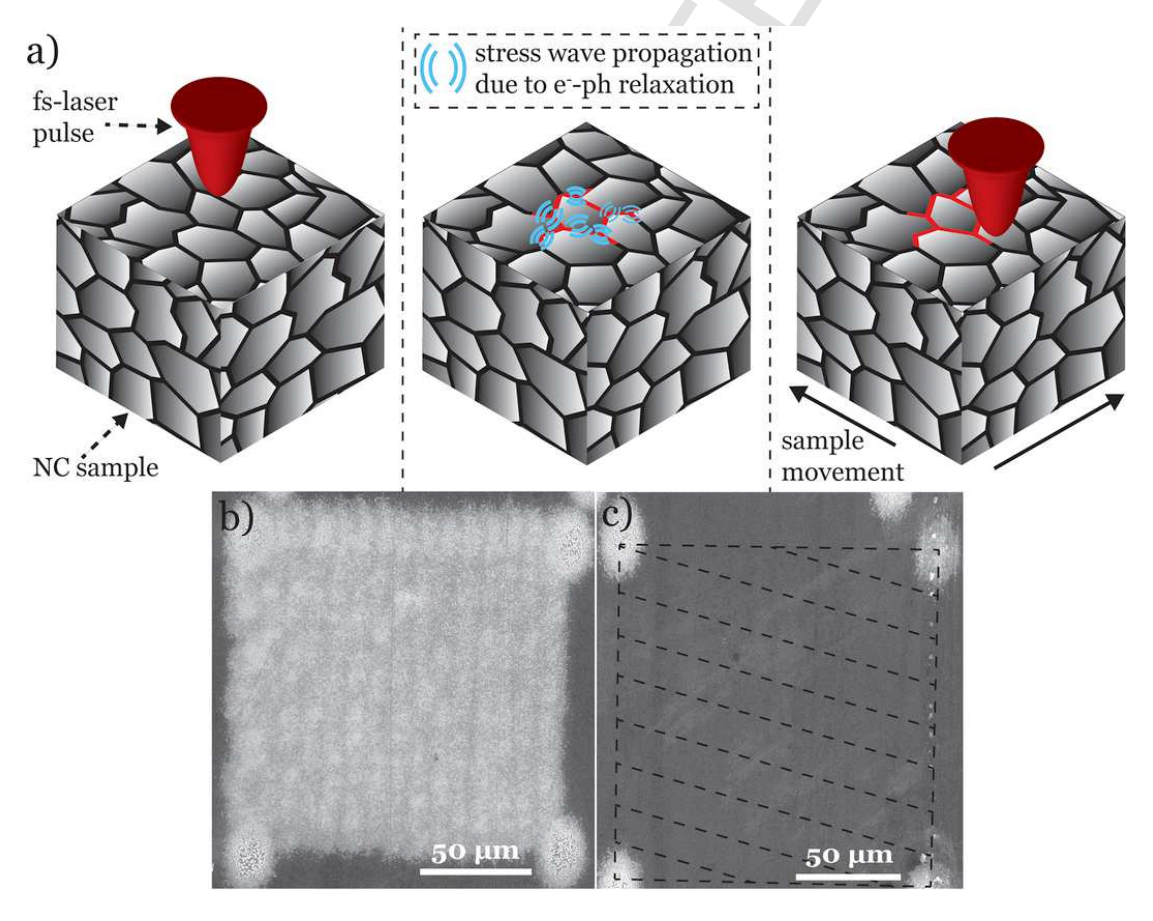


Fig. 2. a) Schematic showing the fs-laser treatment procedure. A single fs-pulse irradiates the NC sample, which then emits elastic waves. Once this process has completed, the sample is translated and irradiated with a series of pulses until the desired irradiated area is reached. b) SEM image of the Al-4.8 at.%O sample irradiated with a fluence above the ablation threshold. The four lighter areas on the corners of the square are fiducial marks. c) SEM image of the Al-4.8 at.%O sample irradiated with a fluence below the ablation threshold. Dashed lines indicate region that has been irradiated.

ter all experiments to ensure that the tip area functions had not changed significantly throughout the course of the test. All data was collected operating the machine using the continuous stiffness method (CSM), where a dynamic oscillation is superimposed during loading to measure hardness and elastic modulus as a function of depth [61]. For the thin Al films, while extracting true properties of the film is non-trivial, we adopt the Saha-Nix approach [62] and extract values from ~30% of the film thickness. Changing the depth at which the hardness is extracted by 10 nm leads to a 10% change in the hardness value for the Al-4.8 at.%O sample, but relative changes in hardness between laser irradiated areas were only marginally influenced. This suggests that any reported change in hardness, ΔH , represents a lower bound of the actual magnitude change, and the relative change between different laser treated areas is not significantly affected by the depth chosen to extract measurements. Each data point plotted below corresponds to at least 20 indentations, and test locations were chosen to be towards the interior of irradiated regions to minimize non-uniformities in the laser profile due to overlapping pulses. The predominant source of error in the nanoindentation measurements of thin Al films reported is surface roughness, which has been analyzed extensively by He et al. [22].

Electron transparent samples of the Al-4.8 at.%O in both irradiated and unirradiated conditions were prepared using a FEI Helios Dualbeam Nanolab 650 focused ion beam (FIB) with a final ion polishing step at 5 kV, 16 pA to remove FIB-induced damage. Sample thicknesses were approximately 150 nm. Transmission scanning electron microscopy (TSEM) [63] images were made using an FEI Teneo field-emission scanning electron microscope (FESEM) operating at 30 kV, 0.4 nA, and equipped with an annularly-segmented scanning transmission electron microscopy detector.

3. Sample selection

Samples were deliberately selected to give insight into the effects of grain size, chemistry, and GB energy state on sub-ablation threshold fs-laser treatments. The two NC Al samples demonstrate the effect of grain size and solute concentration. The grain size of these samples can be controlled during deposition by varying the amount of O incorporated, which serves to pin GBs. This behavior and the effect of O impurities on the mechanical behavior of Al films has been shown extensively in Ref. [22]. Comparison between the Cu-Zr samples enables us to explore the effects of the initial GB state on fs-laser treatments for a fixed grain size, as both O-Cu-Zr and SC-Cu-Zr have the same chemistry and grain size. Comparing the effects of sub-ablation threshold fs-laser irradiation on these alloys to the Al samples provides insight across material systems. Due to the two sample preparations for the Cu-Zr alloy – quenching and slowly cooling from high temperature - the samples possess different initial GB states. The quenched sample possesses an AIF, which is a metastable, non-equilibrium GB structure at room temperature where the laser treatments are performed. AIFs are at equilibrium at elevated temperature and form in these alloys due to the propensity for Zr to segregate to GBs, which reduces the energetic penalty for the formation of an amorphous film. The amorphous structure is thought to form at GBs due to the interfacial energy and the locally high concentration of Zr in Cu, which is a good glass forming alloy [57]. The slowly-cooled sample, however, possesses atomically thin GBs, which are near equilibrium at room temperature. Any treatment used to modify the energy of a boundary would be expected to be sensitive to the initial energetic configuration, which would manifest as different mechanical responses.

4. Results

4.1. Hardness variations

We first begin by investigating the effects of grain size in the NC Al samples on the hardness measured before and after fs-laser irradiation. Fig. 3a shows the hardness of the coarsest grained Al-0.8 at.%O sample (average grain size of 80 nm) irradiated by the fs-laser at various sub-ablation fluences, and indicates no significant variation in the hardness. Deviations from the initial hardness are observed after the onset of ablation, and the variability in these measurements also increases. The ablation threshold of the Al-0.8 at.%O sample occurred at a fluence of $0.2\pm0.02\,\mathrm{J\,cm}^{-2}$. This agrees well with literature values for fs-laser ablation of Al, which range from 0.1 to 0.19 J cm suggesting that dilute amounts of oxygen incorporation do not dramatically affect the ablation threshold compared to pure Al [55,64]. Fig. 3b shows the hardness of the Al-4.8 at.%O sample after similar laser treatments, where a dramatic decrease in hardness of up to 80% (~2 GPa) is observed at energies nearing the ablation threshold. The hardness of the Al-4.8 at.%O monotonically decreases with increasing laser fluence. The inset shows several representative load-displacement curves from the untreated and 0.066 J cm⁻² treated region, where the peak load is significantly lower for the fs-laser irradiated sample. The ablation threshold was measured at $0.15\pm0.02\,\mathrm{J\,cm}^{-2}$, 25% lower than the Al-0.8 at.%O sample. While decoupling the effects of impurity incorporation and grain size are difficult for these samples, this result suggests that either the reduction in grain size or increased O content, or some combination thereof, determines the material susceptibility to fs-laser-induced changes in hardness and ablation behavior.

The influence of GB state on the mechanical response of samples subjected to sub-ablation-threshold fs-laser irradiation was investigated in the Q- and SC-Cu-Zr samples. These samples have nominally identical chemistries and grain sizes, but with different GB structures. Fig. 3c shows the effects of fs-laser irradiation on the Q-Cu-Zr sample possessing AIFs, which manifests as up to a \sim 60% (\sim 1.6 GPa) maximum reduction in hardness, and Fig. 3d shows the fs-laser effects on the SC-Cu-Zr sample, which exhibits up to a \sim 80% (\sim 2.5 GPa) decrease in hardness. In all cases, the reduction in hardness monotonically increases with fluence up to a saturation value near the ablation threshold. Hardness values in Fig. 3 (c, d) were extracted from depths of $40\pm5\,\mathrm{nm}$ in order to capture the near-surface effects of the laser. Both Q-Cu-Zr and SC-Cu-Zr have similar initial hardness values, which is consistent with previous investigations of these materials, Ref [57], that report a 10% difference in yield strengths between the two samples. An analysis of the changes in hardness as a function of depth will be presented in the following section. The ablation thresholds of the Q-Cu-Zr and SC-Cu-Zr samples were $0.33\pm0.02\,\mathrm{J\,cm}^{-2}$ and $0.5\pm0.02\,\mathrm{J\,cm^{-2}}$, respectively (Table 1). This difference in ablation thresholds will be discussed further, as, unlike the Al-O samples, these samples have nominally the same grain size and chemistry, so any difference in their ablation behavior is only due to the different GB structures present in the different samples.

4.2. Depth dependence

To better characterize the intrinsic bounds of the laser induced change in hardness, we frame our results in terms of the geometries of each sample. The two features of the geometry in question are (i) the microstructure – grain size and GB thickness – and (ii) the optical

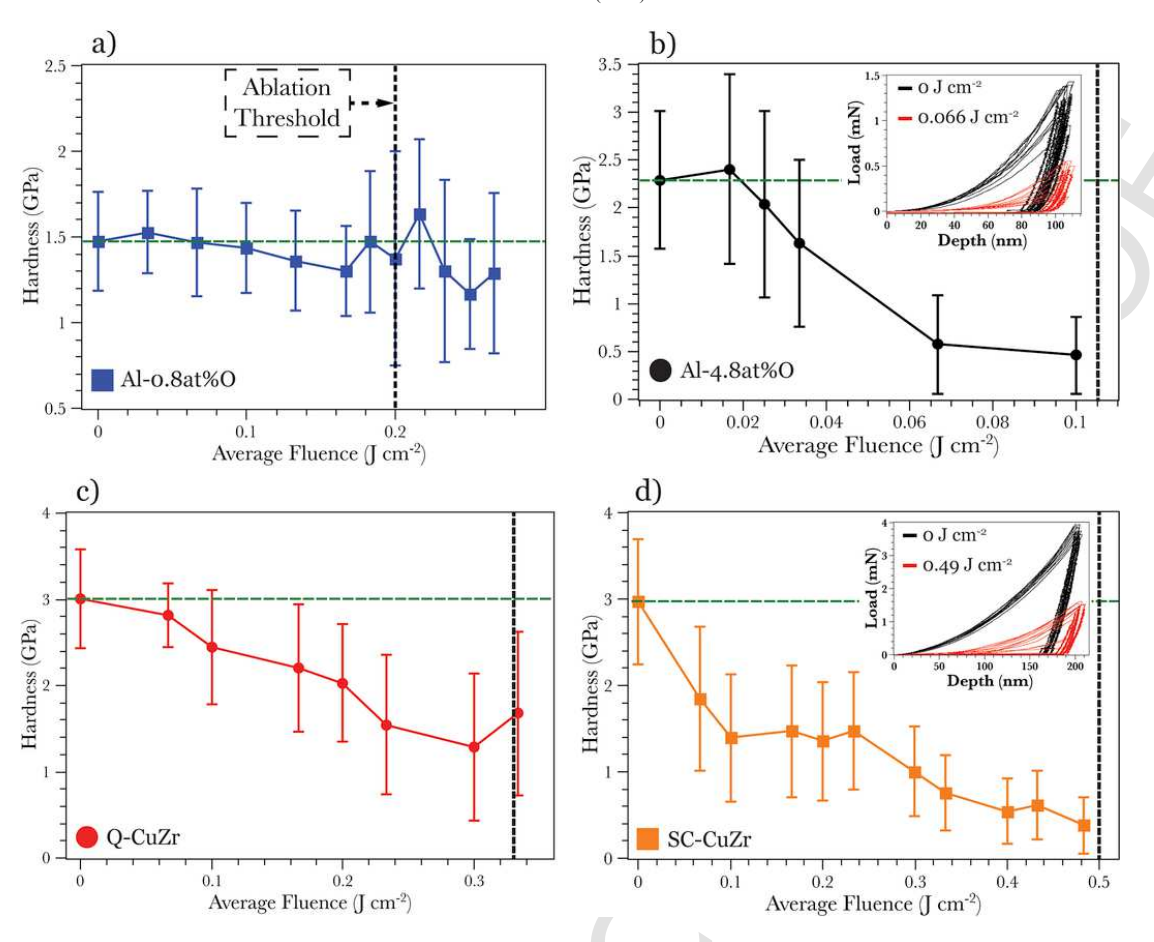


Fig. 3. Hardness measured by nanoindentation as a function of laser fluence for all samples. The green horizontal dashed line is the mean hardness of the non-irradiated sample, and the ablation threshold is denoted by the vertical dashed line. a) Al-0.8 at.%O, b) Al-4.8 at.%O, and several representative load-displacement curves for the untreated and 0.066 J cm⁻² treated regions. c) Q-Cu-Zr. d) SC-Cu-Zr, and several representative load-displacement curves for the untreated and 0.495 J cm⁻² treated regions. All data plotted in b-d are at energies below the ablation threshold (vertical dashed line) for each material. (For interpretation of the references to colour in this figure legend, the reader is referred to the Web version of this article.)

penetration depth of the laser. To do this, we investigate the depth dependence for all samples, with a focus on the Cu-Zr samples, as their bulk form simplifies the interpretation compared to the NC Al films on substrates. The laser predominantly interacts with the material in the optical penetration depth for 780 nm wavelength light, which can be calculated using $\delta = 1/\alpha = \lambda/(4\pi\kappa)$, where δ is the optical penetration (or skin) depth, α is the optical absorption coefficient, λ is the wavelength of irradiation and κ is the extinction coefficient. Appropriate parameters are located in Table 1. κ for the Cu-Zr samples was calculated using a rule of mixtures, $\kappa_{AB} = X_A \kappa_A + X_B \kappa_B$ where κ_A and κ_B are the extinction coefficients of the pure metals from Refs. [65–67], and κ_B are the compositional ratios of κ_B and κ_B respectively.

While the stress state resulting from fs-laser-matter interactions is complex and not strictly confined to this skin depth, we expect the largest effect in this region. Simulations predict a lower ablation threshold for certain amorphous Cu-Zr compositions compared to their crystalline counterparts [56], and also a lower ablation threshold for NC Al compared to single crystalline Al [55], so we posit that the total GB "volume" influenced by the laser will be important in understanding the resultant mechanical deformation. By assuming an average grain size, shape, GB thickness, and approximate plastic zone, we calculate several quantities of interest – (i) an approximate volume of

material probed via indentation, (ii) the volume of GB regions probed, (iii) the volume of probed materials and GBs that are within the optical skin depth, as well as (iv) the volume fraction of "affected" GBs, defined as the ratio of the volume of boundaries within the optical skin depth of the plastic zone to the volume of boundaries probed in the plastic zone of the indenter. For the following calculations, we assume cuboidal grains with side lengths equal to the average grain size and a constant GB thickness for each material. For the Cu-Zr samples, TEM measurements of GB thicknesses from Ref. [57] of 3 nm for the AIFs in Q-Cu-Zr and 0.5 nm for the ordered GBs in SC-Cu-Zr are used. As previously mentioned, a range of AIF thicknesses exists within any given sample. For reference, a typical distribution of AIF thicknesses for this sample is presented in Ref. [57], and AIF thicknesses of roughly 3 nm were most commonly observed. We assumed a GB thickness of 0.5 nm for both Al samples, consistent with other measurements of GB thickness in the literature [68-70]. Schematically this is shown in Fig. 4, where the gray regions depict grain interiors and black regions GBs. The plastic zone size probed during indentation was assumed to be a hemisphere with radius r = 1.9a where a is the contact radius of the tip at the prescribed depth [71]. Additionally, to compare different samples and analyze intrinsic material effects, we normalize the hardness as follows

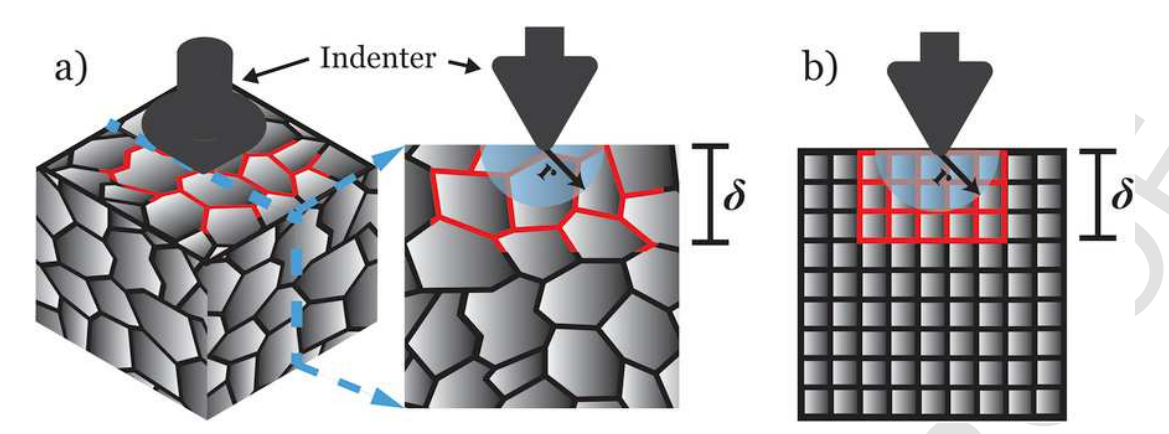


Fig. 4. a) Schematic showing NC sample being mechanically deformed with an indenter and corresponding vertical cross-section. The red region indicates part of the sample that has been irradiated with the laser. The light blue shaded hemispherical region with radius r is the approximate plastic zone of the indenter, and δ is the optical penetration depth of the laser. b) shows the approximate geometry used to calculate a volume fraction of GBs affected and probed. (For interpretation of the references to colour in this figure legend, the reader is referred to the Web version of this article.)

$$\frac{\Delta H}{H} = \frac{H\left(\phi\right) - H\left(\phi = 0\right)}{H\left(\phi = 0\right)} \tag{1} \label{eq:deltaH}$$

where $H(\phi)$ is the hardness of the material exposed to single pulse fs-laser pulses at fluence ϕ . Fig. 5 shows the normalized change in hardness as a function of the volume fraction of affected boundaries for all samples. The data in Fig. 5 was extracted from regions with the largest change in hardness in Figs. 3–0.178 J cm⁻² for the Al-0.8 at.%O, 0.1 J cm⁻² for Al-4.8 at.%O, 0.3 J cm⁻² for Q-Cu-Zr, and 0.49 J cm⁻² for SC-Cu-Zr. Fig. 5 indicates that, when normalized by the geometric constraints of the samples, the observed softening appears to saturate at a threshold level of affected GB volume fraction of $\sim 5 \times 10^{-5}$. We investigated this behavior at all sub-ablation flu-

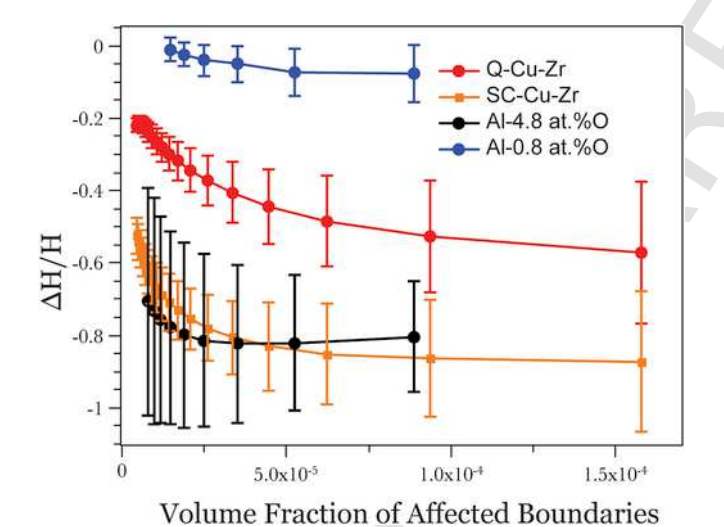


Fig. 5. Normalized change in hardness as a function of volume fraction of affected GBs for all samples. Data presented here was extracted from indentation measurements from regions with the largest change in hardness in Fig. 3–0.178 J cm $^{-2}$ for the Al-0.8 at.%O, 0.1 J cm $^{-2}$ for Al-4.8 at.%O, 0.3 J cm $^{-2}$ for Q-Cu-Zr, and 0.49 J cm $^{-2}$ for SC-Cu-Zr. Hardness reduction for the Al-4.8 at.%O, SC-Cu-Zr, and Q-Cu-Zr saturate near a volume fraction of $\sim 5\times 10^{-5}$. The saturation behavior suggests that the effects of the laser are spatially constrained to surface GB regions, and there is an intrinsic upper bound on the change in hardness associated with the fs-laser treatments. Similarities in the magnitudes of the normalized change in hardness for the Al-4.8 at.%O and SC-Cu-Zr suggest both samples are low energy reference configurations.

ences using the same analysis, and, for a given sample, the salient feature is that the saturation threshold is constant, despite the different magnitudes of softening. The relative magnitudes of the softening between samples also depend on the initial reference state of each sample. The Al-0.8 at.%O exhibits an insignificant change in hardness at all depths and sub-ablation fluences, whereas the Al-4.8 at.%O and SC-Cu-Zr exhibit significant softening behavior. The Q-Cu-Zr shows a smaller magnitude of softening, but exhibits similar trends compared to the Al-4.8 at.%O and SC-Cu-Zr samples.

5. Discussion

Our results presented thus far have indicated that (i) sub-ablation threshold fs-laser irradiation causes dramatic (up to 80%) reductions in hardness in the NC alloys (Al-4.8 at.%O, Q- and SC-Cu-Zr) with very fine grain size (<50 nm), (ii) negligible changes in hardness of larger grain NC sample (Al-0.8 at.%O), and (iii) a strong dependence on the geometry of the samples and fs-laser-material interaction. To better understand these results, we begin by discussing the sample with the largest grain size, where laser-material interactions are largely in the grain interiors.

5.1. Influence of grain boundaries

Fig. 3b indicates no significant change in hardness of the Al-0.8 at.%O sample with increasing laser fluence. What differentiates this sample from the others in this study is the larger grain size and smaller concentration of alloying additions (see Table 1). Performing the same geometric analysis as above, the Al-4.8 at.%O possesses a GB volume fraction of \sim 7.5%, whereas the Al-0.8 at.%O has a GB volume fraction of $\sim 2\%$. The calculated optical penetration depth for both of these samples is 7.3 nm, suggesting a smaller "affected" volume of GB for the Al-0.8 at.%O samples. Compared to the other samples, particularly the Al-4.8 at.%O, which exhibit a large decrease in hardness, the absence of any change in hardness in the Al-0.8 at.%O is noteworthy because it suggests that (i) the fs-laser interactions that cause softening in the other samples occur predominantly at GBs, that (ii) vacancy or Frenkel pair formation within the grain interior is not responsible for the changes in mechanical properties of the other samples, and that (iii) residual stresses and dislocation activity induced by the laser are not responsible for the softening in other samples. We discuss each of these mechanisms in detail below.

Due to the relatively large grain size of this sample (80 nm, primarily due to the smaller amount of oxygen that decorates GBs [72,73]), and the smaller volume of GBs both affected by the fs-laser and probed during indentation, the absence of a dramatic change in hardness in this sample indicates that GBs are responsible for the softening observed in other samples. This suggestion is further corroborated by the results of molecular dynamics (MD) simulations [55] indicating that energy deposition caused by the laser occurs differently due to the presence of GBs, due to locally different electron-phonon (e-ph) coupling behavior. This will be discussed further in Section 5.4.

Iyer et al. [74] showed using density functional theory (DFT) that the formation enthalpy of point defects such as monovacancies, self-interstitials, and Frenkel pairs is dramatically reduced under high hydrostatic tensile stresses. The authors in Ref. [74] suggest that fs-laser ablation via void coalescence and spallation may be facilitated by point defect formation under the large hydrostatic stresses induced by the fs-laser. The DFT calculations suggest that the critical hydrostatic tensile stress for vacancy formation is 9 GPa in Al. Atomistic simulations from Gill-Comeau and Lewis [55] suggest that, while the maximum pressure induced by the fs-laser may reach values of close to 9 GPa prior to the onset of ablation in NC Al, the maximum tension is much lower, below 3 GPa. This, coupled with the lack of change in hardness of the Al-0.8 at.%O sample as compared to the Al-4.8 at.%O sample, suggests that the change in mechanical properties is unrelated to point defect formation within the grain interiors due to tensile hydrostatic stresses. In contrast, local atomic displacements and defects may be induced at higher energy sites, such as GBs or triple points, at lower tensile hydrostatic stresses experienced during sub-ablation fs-laser irradiation. Taken as a whole, it is evident in this relatively large-grained sample that any lattice defects introduced by the laser interactions play a negligible role in controlling hardness.

Nanoindentation measurements of hardness are quite sensitive to residual stresses [75]. The presence of tensile residual stresses due to fs-laser irradiation have not been documented in the literature, however compressive residual stresses have been observed during ablation [76]. Samples under a biaxial tensile residual stress show a strong softening behavior in nanoindentation [75]. However, due to the absence of any change in mechanical response of the Al-0.8 at.%O sample, the injection of residual stresses into this material from sub-ablation threshold fs-laser treatments is not a viable explanation for the observed softening.

5.2. Potential softening mechanisms

To explain the laser-mediated observed softening effect in the Al-4.8 at.%O and Cu-Zr samples, we hypothesize four potential mechanisms that could cause the observed decrease in hardness: (i) grain growth, (ii) nucleation and coalescence of porosity, (iii) (de)segregation of solute atoms, and (iv) GB rejuvenation - subtle atomic rearrangements at boundaries akin to rejuvenation in amorphous alloys.

Fs-laser ablation is thought to be caused by mechanical spallation rather than melting or evaporation, which occur too slowly and with too large of a damaged zone to be responsible for ultrafast laser ablation [47]. However, thermal effects are present and should not be ignored, especially at low fluences and high pulse numbers [77,78]. Due to the propensity for grain growth of NC metals both due to thermal loads and stress, coarsening may be responsible for the observed softening seen in Fig. 3. To examine any coarsening due to fs-laser treatments, TSEM [63] was performed on the Al-4.8 at.%O sample. Fig. 6a shows the microstructure of the as-deposited Al-4.8 at.%O. Fig. 6b shows the microstructure of the 0.066 J cm⁻² laser treated Al-

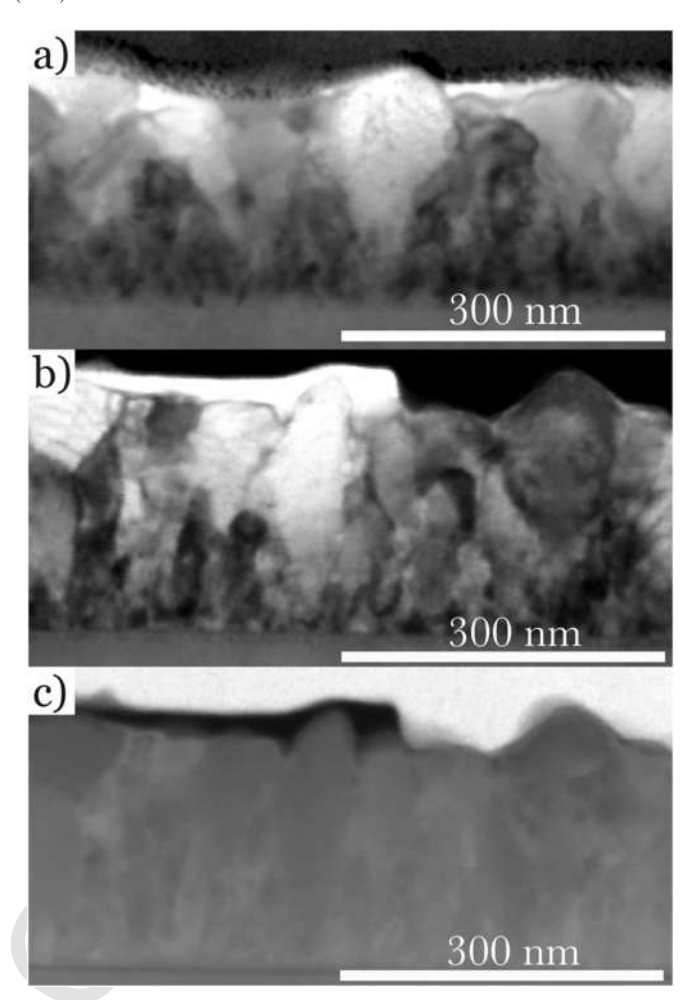


Fig. 6. a) BF TSEM image of a cross section of the untreated Al-4.8 at.%O sample. b) BF TSEM image of a cross section of the 0.066 J cm⁻² treated Al-4.8 at.%O sample, the fluence that corresponds to the maximum change in hardness observed in this sample. C) HAADF TSEM image of a cross section of the 0.066 J cm⁻² treated Al-4.8 at.%O sample. The fs-laser irradiation direction is from the top.

4.8 at.%O. No obvious grain growth is seen in these images, certainly not corresponding to the magnitude predicted by a simple Hall-Petch analysis [79–82]. Based on this analysis and the TSEM images, we conclude that softening due exclusively to grain growth is not a reasonable explanation for the observed behavior.

Fig. 6c shows a high angle annular dark field (HAADF) TSEM image of the 0.066 J cm⁻² laser treated Al-4.8 at.%O. HAADF is sensitive to local chemistry and mass-thickness product of the sample [83], so porosity would manifest as dark regions in the image. Fig. 6c indicates no obvious porosity due to fs-laser irradiation. While simulations [54] indicate that subsurface porosity generation is possible during femtosecond laser ablation under some conditions, we see no evidence of this occurring here. Fig. 6c contains slight differences in intensity within the sample, predominantly due to different grain orientations and concentration of O at GBs, which has been previously investigated in these samples by atom probe tomography [22,73]. These observations suggest that evolution of porosity is not the dominant mechanism behind the observed softening.

Much of the strength and stability of these NC alloys can be attributed to solute (O for the Al-4.8 at.%O, and Zr for the Cu-Zr samples) located at the GBs that serves to stabilize the nanostructure and mediate GB-based deformation mechanisms. Recent work by Hu et

al. [3] indicated that annealing-induced GB segregation of Mo in NC Ni-Mo alloys resulted in increases in hardness of several GPa for all samples tested with only moderate increases in grain size. The most dramatic change shown in Ref. [3] was for the highest Mo concentration studied (Ni-21.5 at.% Mo), which underwent a 128% increase in hardness from ~4.9 GPa to 11.2 GPa. Thus, the mechanical properties of this system can be tied to the GB structure and solute excess. If the GB structure were to be modified by forcing some solute atoms into the interior of the grain, i.e. desegregation, this could manifest as softening. For this to be a measurable effect, it requires that the structure not relax to its initial state prior to indentation – i.e. a solute atom displaced by the laser could not segregate back to the GB at room temperature. Looking at the Al-4.8 at.%O sample, we see that this diffusion time is far too short to produce a measurable effect.

While diffusion coefficients of O in Al are difficult to measure experimentally, we expect the diffusivity to be generally faster than that of Oxygen in α -Al₂O₃, which we will use as a lower bound. At room temperature, we calculated a lower bound diffusion coefficient of $D_0 = 4.29 \text{ cm}^2 \text{ s}^{-1}$ using the model proposed in Ref. [84]. Assuming a diffusion depth of $x \approx \sqrt{4D_0t}$, and an average grain size of 20 nm, the time needed for the solute to diffuse back to a GB would be $t \approx \frac{x^2}{4D_0} \approx \frac{(20 \text{ nm})^2}{4D_0} < 2X10^{-13} \text{s}$, which implies that any interstitial O displaced as a result of fs-laser irradiation would have diffused to the GB in the time between the laser treatment and indentation. Hence, we conclude that this type of chemical effect is not responsible for the softening we measure.

5.3. Rejuvenation

We thus hypothesize that the observed softening caused by the fs-laser is mechanistically rooted in the high local stresses at GBs produced by the fs-laser, which induce short-range atomic rearrangements that serve to decrease the apparent hardness. We adopt the term rejuvenation to echo similar descriptions utilized in the MG community, where rejuvenation processes have been shown to elicit dramatic softening measured by a decrease in hardness and modulus, as well as the potential for tensile ductility [42]. Rejuvenation in the MG community has been described as an increase in the overall energy of the system by occupying higher-energy metastable structural states [42]. This mechanism concentrated at GB regions is predicated on the existence of a multiplicity of inherent metastable structural configurations, as recently suggested by Refs. [14,15]. This process is akin to rejuvenation processes employed by the MG community, which induces softening and suppresses catastrophic shear localization. The effect of rejuvenation processes in MGs depend upon the initial energy state, and are also completely recoverable through subsequent relaxation treatments such as low temperature annealing [40,42]. Drawing these parallels to fs-laser irradiation of NC metals, we explore the effects of the initial energy state between the SC-Cu-Zr and Q-Cu-Zr samples, as well as the effects of low temperature annealing performed on the SC-Cu-Zr and Al-4.8 at.%O.

5.4. Initial energy state

Fig. 5 allows us to compare the effects of fs-laser treatments on two samples with the same chemistry but different initial energy states – the Cu-Zr alloy samples. The Q-Cu-Zr sample with amorphous boundaries represents a high-energy, non-equilibrium initial state, whereas the SC-Cu-Zr samples exhibit GB structures closer to equilibrium. Since rejuvenation processes raise the energy of the system, driving it further from equilibrium, we expect that the Q-Cu-Zr

sample will have a smaller magnitude change than the SC-Cu-Zr subject to any rejuvenation process. Simulations of amorphous solids have shown the presence of distinct solid-like and liquid-like atomic structures, and that the relative fraction of solid-like and liquid-like environments can be tailored through various processing, such as different cooling rates [84]. The higher energy states of the solid will exhibit more liquid-like environments, and when the material is composed of completely liquid-like structures, it is effectively a supercooled liquid. In our case, the fs pulses of energy are being utilized to drive the system energetically uphill, and a large volume fraction of initially liquid-like structures may drive the system toward an earlier onset of ablation. Fig. 5 indicates that the Q-Cu-Zr exhibits a smaller magnitude of the saturation $\Delta H/H$ than the SC-Cu-Zr. Furthermore, the ablation threshold of the SC-Cu-Zr sample is approximately 50% higher than the Q-Cu-Zr. Both of these observations are in line with the supposition that sub-ablation threshold fs-laser treatments can be understood as a rejuvenation process, and can also be reconciled by considering the physics of the fs-laser-material interactions. Namely, these interactions rely on the disparity between electronic excitation, which occurs in fs, and phononic relaxation, which occurs in ps. Thus, in materials with heterogeneous atomic structures, there may be heterogeneous relaxation behavior due to locally different electron-phonon (e-ph) coupling. In the Cu-Zr alloys, this plays a significant role. It has been shown in MD simulations that disordered CuZr₂ has an e-ph collision rate that is over an order of magnitude larger than pure Cu, and an e-ph coupling factor double that of pure Cu at low temperatures [56]. This difference in e-ph coupling times in amorphous and crystalline Cu-Zr may lead to locally higher energy deposition in regions with the stronger e-ph coupling and shorter e-ph coupling time. The role of GBs on e-ph coupling times and strength is debated in the literature [55,86,87]. Gill-Comeau and Lewis [55] performed MD simulations of fs-laser ablation for NC Al, accounting for the effects of GBs on e-ph coupling, and found that NC Al has an earlier onset of ablation than single crystal Al, in general agreement with our experimental results here. We suggest that, similar to the analysis performed by Ref. [55], GB regions have characteristically larger e-ph coupling factors and shorter equilibration times. This implies that the fs-laser affords the unique ability to locally deposit energy at GB regions. As a consequence, the higher volume fraction of amorphous material localized at GB regions in the Q-Cu-Zr sample would exhibit an earlier onset of ablation, as there is a faster and more dramatic electronic relaxation process occurring in this material. The SC-Cu-Zr sample has a smaller volume of disordered material, and would be expected to have a higher ablation threshold – in agreement with our observations.

The smaller magnitude $\Delta H/H$ in the Q-Cu-Zr can be reconciled as follows: if we envisage that the laser causes small structural changes in the GBs that drive them further from equilibrium, the sample with a relaxed (more equilibrium) GB structure will be able to access more metastable, high-energy configurations, compared to an initially non-equilibrium, high energy GB structure. In other words, occupying a deeper position in the basin of the energy landscape provides ample room for moving energetically uphill. This broader range of metastable states implies a larger $\Delta H/H$. This also follows logically from an e-ph relaxation perspective - small atomic rearrangements in the amorphous region where the majority of the e-ph equilibration occurs would not necessarily lead to drastic differences in mechanical behavior, as the formation of a shear band is suppressed at these length scales [87]. Thus, prior to the onset of ablation, a smaller change in hardness is expected in the Q-Cu-Zr sample than the SC-Cu-Zr. This is seen in Fig. 5, where the Q-Cu-Zr undergoes a 57% reduction in hardness, whereas the SC-Cu-Zr undergoes an 87% reduction

Fig. 5 also shows the normalized change in hardness for the Al samples. Interestingly, the GB volume dependence and normalized change in hardness of the Al-4.8 at.%O and SC-Cu-Zr are quite similar in this plot. This can be ascribed to both samples containing initially relaxed, low energy GB configurations. The Al-4.8 at.%O, despite its fine grain size, is stabilized by the high solute concentration, evidenced by the apparent mechanical stability of this sample [22]. A similar interpretation for the SC-Cu-Zr can be inferred owing to its thermal history and the tendency for Zr segregation to GBs.

5.5. Relaxation annealing

Annealing experiments were performed on the irradiated Al-4.8 at.%O and SC-Cu-Zr samples to determine if the observed decrease in hardness is recoverable. Since AIFs are only in equilibrium at very high temperature and are kinetically frozen in at room temperature, an annealing treatment would likely remove any AIFs present. Therefore, we do not anneal the Q-Cu-Zr sample here. All heat treatments were performed in a quartz tube furnace in an Ar environment ($<10^{-8}$ ppm O_2) to minimize additional oxidation. The Al-4.8 at.%O film was annealed for 90 min at 205 °C. The SC-Cu-Zr sample was annealed for annealed for 120 min at 350 °C. Temperatures were chosen to be $\approx 0.5 \, T_m$, slightly higher than other relaxation heat treatments reported for NC metals [3,23–25]. Relaxation annealing tem-

peratures are chosen to be low enough to preclude grain growth, but high enough to allow short-range diffusive atomic rearrangements, predominantly at GBs where the structural disorder and diffusivities are much higher. The higher temperature range was selected due to the apparent thermal stability of these samples, owing to the high propensity for solute segregation in these material systems [57,58,73]. To ensure that the microstructure does not undergo coarsening during this annealing treatment, TEM investigations of grain size were conducted. The average grain size of the Al-4.8 at.%O after annealing was $22 \pm 9 \,\mathrm{nm}$, and the average grain size of the SC-Cu-Zr after annealing was $44 \pm 16 \,\mathrm{nm}$. We note no significant coarsening of the microstructure or recrystallization after annealing at these modest temperatures.

Indentation tests were performed on the same regions before and after annealing to elucidate any changes in mechanical properties caused by the heat treatment. Fig. 7(a and b) show the hardness measurements of the Al-4.8 at.%O and SC-Cu-Zr samples conducted before and after relaxation annealing, with the duration and homologous temperatures of the heat treatment indicated in each plot. The green horizontal dashed line indicates the mean initial, non-irradiated hardness measured for each of the two samples. Annealing returned the hardness of the Al-4.8 at.%O to 2.44 GPa, compared to a hardness of 0.57 GPa after irradiation, and the SC-Cu-Zr to 2.87 GPa, compared to a hardness of 0.77 GPa after irradiation. These results indicate that the effect caused by the fs-laser treatments is fully reversible upon annealing, and the initial mechanical properties of the samples are re-

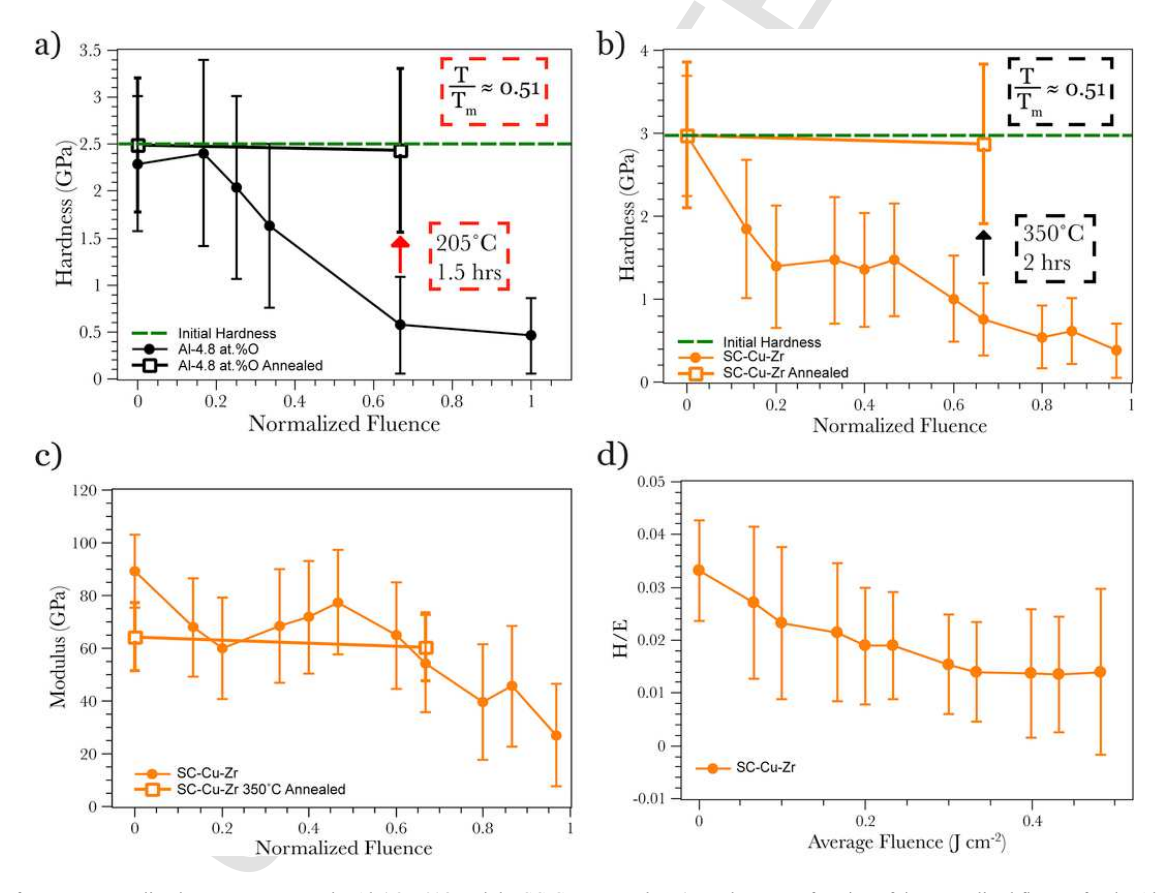


Fig. 7. Effects of recovery annealing heat treatments on the Al-4.8 at.%O and the SC-Cu-Zr samples. a) Hardness as a function of the normalized fluence for the Al-4.8 at.%O sample. Normalized fluence is the measured fluence divided by the ablation threshold for each material. Filled black circles indicate the material prior to annealing, and the open black squares are the measurements conducted after annealing at 205 °C for 1.5 hb) Hardness as a function of normalized fluence for the SC-Cu-Zr sample annealed at 350 °C for 2 h. Initial measurements prior to annealing are indicated by filled in orange circles, whereas measurements performed after annealing are shown as open orange squares. c) Shows the measured modulus for the SC-Cu-Zr sample annealed at 350 °C for 2 h as a function of normalized fluence, and d) shows the ratio of the hardness to the modulus as a function of average fluence for the same sample. (For interpretation of the references to colour in this figure legend, the reader is referred to the Web version of this article.)

covered. By recovering the same hardness value as the initial non-irradiated samples, we can conclude that the initial energy state of both the Al-4.8 at.%O and SC-Cu-Zr samples is relatively low, and any effects induced by the fs-laser can be reversed through boundary-mediated mechanisms operative at low temperatures. Fig. 7c shows the modulus data for the SC-Cu-Zr sample, indicating that the fs-laser induces small changes in modulus. It appears that the two areas probed after annealing have statistically insignificant changes in modulus. The recoverability of the mechanical response after low temperature annealing further proves that grain growth and evolution of porosity are not responsible for the change in mechanical properties, as the temperatures for this annealing treatment were not high enough to remove porosity or coarsen the grains. Further kinetic studies are necessary to fully characterize this relaxation process and identify activation energies associated with the rate-limiting mechanisms.

5.6. Mechanisms of NC fs-laser mediated rejuvenation

We hypothesize that several mechanisms may be operative in eliciting rejuvenation, but they are all predicated on the physical underpinning of local atomic shuffling leading to metastable GB configurations. This phenomenon can be represented in a number of ways – accessing various micro degrees of freedom at GBs [14], civilian or military shuffling modes at GBs [9], GB structural transitions [27,89], modification of disconnection densities [90], or shear transformation zone (STZ)-like activity [32,91,92]. Han et al. [14] show using MD simulations that a bicrystal can exhibit many metastable GB structures for a given misorientation. The high stresses involved during fs-laser processes may be sufficient to modify the structure of GBs, as suggested by Iyer et al. [74]. While Ref [74] focuses on point defect formation, they argue that at GBs or other high-energy sites, the critical stress needed to form a vacancy or Frenkel pair may decrease to be energetically favorable from stresses induced by the fs-laser. The presence of these defects along a GB may change the atomic structure of the boundary to a higher energy configuration. Similarly, the high stresses may enable other shuffling modes at GBs [9], which also enable the formation of high-energy GB structures. The presence of metastable GB structures has been shown to affect the operative deformation mechanisms, favoring grain boundary sliding, void formation and intergranular cracking [93]. STZ-like activity at GB regions of NC metals has been reported for materials with small grain sizes [32,91,92,94], where STZs can coalesce to form a catastrophic shear band. Recent results showing that the size of correlated regions participating in STZ-like rearrangements is of the order of the particle diameter (atomic size) [95] lends credence to the idea that rearrangements can occur even in spatially constrained GB regions. Activation of STZ-like mechanisms during deformation would significantly decrease the strength of a material, as evidenced by the softening behavior of NC metals commonly observed at very fine grain sizes [91]. Given the subtlety of the structural changes occurring at the atomic scale at GBs, advanced characterization methods will be needed to elucidate the differences in atomic configurations responsible for the changes in mechanical behavior.

6. Conclusions

Our mechanical measurements and characterization of NC Al-O and Cu-Zr alloys subject to sub-ablation threshold fs-laser treatments allow us to draw the following conclusions:

 Nanoindentation measurements indicate that sub-ablation-threshold fs-laser treatments cause a significant decrease in hardness in NC metals with grain sizes finer than 50 nm.

- The induced softening can be ascribed to the fs-laser interaction with grain boundary regions, due to structural and chemical heterogeneities. Coarsening, porosity, and segregation effects can be ruled out as causes for the softening.
- The reduction in hardness is depth dependent, and consistent across samples normalized for grain boundary volume.
- The magnitude of softening caused by the fs-length laser pulses is dependent upon the initial energetic state of the material – samples with non-equilibrium grain boundary structures had a smaller magnitude softening prior to ablation, whereas samples near equilibrium had large tunability in hardness.
- The softening induced by the fs-laser is fully recoverable upon annealing at low temperatures, suggesting that atomic motion at grain boundary regions (operative at such low temperatures) is responsible for both the softening and relaxation. The fs-laser treatment evidently concentrates its deposition of energy in grain boundary regions possessing disorder, with minimal impact to the crystalline grain interiors.

This study suggests that the similarities between NC metals and amorphous alloys are vast, and that our understanding of mechanical behavior of NC metals may be greatly informed by the MG community. The application of processing strategies across disciplines, such as fs-laser processing, and material classes can be useful in broadening the tunability and functionality of NC materials. The premise of structural rejuvenation of NC metals and its impact on properties such as ductility and damage tolerance is a promising area for future research.

Uncited references

[85], [88].

Acknowledgements

This work was funded by NSF CMMI-1724519 and supported by a NSF GRFP Award No. 1650114. T.J.R and C.M.G were supported by the U.S. Army Research Office under Grant W911NF-16-1-0369. The authors would like to thank Chris J. Torbet and David J. Jorgensen for their fs-laser expertise, Verena Maier-Kiener for helpful discussions about indentation analysis, as well as Jean-Charles Stinville, Patrick G. Callahan, and Mark Cornish for their microscopy assistance. The research reported here made use of shared facilities of the UCSB MRSEC (NSF DMR 1720256), a member of the Materials Research Facilities Network (www.mrfn.org). The authors acknowledge the use of instruments at the Electron Imaging Center for NanoMachines supported by NIH (1S10RR23057 and 1S10OD018111), NSF (DBI-1338135) and CNSI at UCLA.

References

- K.S. Kumar, H. Van Swygenhoven, S. Suresh, Mechanical behavior of nanocrystalline metals and alloys, Acta Mater. 51 (19) (2003) 5743–5774.
- [2] L. Lu, X. Chen, X. Huang, K. Lu, Revealing the maximum strength in nanotwinned copper, Science 323 (5914) (2009) 607–610.
- [3] J. Hu, Y.N. Shi, X. Sauvage, G. Sha, K. Lu, Grain boundary stability governs hardening and softening in extremely fine nanograined metals, Science 355 (6331) (2017) 1292–1296
- [4] H. Van Swygenhoven, J.R. Weertman, Deformation in nanocrystalline metals, Mater. Today 9 (5) (2006) 24–31.
- [5] M.A. Meyers, A. Mishra, D.J. Benson, Mechanical properties of nanocrystalline materials, Prog. Mater. Sci. 51 (4) (2006) 427–556.
- [6] T.J. Rupert, C.A. Schuh, Sliding wear of nanocrystalline Ni–W: structural evolution and the apparent breakdown of Archard scaling, Acta Mater. 58 (12) (2010) 4137–4148.

- [7] Z. Shan, E.A. Stach, J.M.K. Wiezorek, J.A. Knapp, D.M. Follstaedt, S.X. Mao, Grain boundary-mediated plasticity in nanocrystalline nickel, Science 305 (5684) (2004) 654–657.
- [8] F. Sansoz, J.F. Molinari, Incidence of atom shuffling on the shear and decohesion behavior of a symmetric tilt grain boundary in copper, Scripta Mater. 50 (10) (2004) 1283–1288.
- [9] H. Van Swygenhoven, P.M. Derlet, Grain-boundary sliding in nanocrystalline fcc metals, Phys. Rev. B 64 (22) (2001), 224105.
- [10] H. Van Swygenhoven, P.M. Derlet, A.G. Frøseth, Nucleation and propagation of dislocations in nanocrystalline fcc metals, Acta Mater. 54 (7) (2006) 1975–1983.
- [11] H. Van Swygenhoven, P.M. Derlet, A. Hasnaoui, Atomic mechanism for dislocation emission from nanosized grain boundaries, Phys. Rev. B 66 (2) (2002), 024101.
- [12] L. Tan, T.R. Allen, J.T. Busby, Grain boundary engineering for structure materials of nuclear reactors, J. Nucl. Mater. 441 (1) (2013) 661–666.
- [13] S. Özerinç, K. Tai, N.Q. Vo, P. Bellon, R.S. Averback, W.P. King, Grain boundary doping strengthens nanocrystalline copper alloys, Scripta Mater. 67 (7) (2012) 720–723.
- [14] J. Han, V. Vitek, D.J. Srolovitz, Grain-boundary metastability and its statistical properties, Acta Mater. 104 (2016) 259–273.
- [15] J. Han, V. Vitek, D.J. Srolovitz, The grain-boundary structural unit model redux, Acta Mater. 133 (2017) 186–199.
- [16] D.S. Gianola, S. Van Petegem, M. Legros, S. Brandstetter, H. Van Swygenhoven, K.J. Hemker, Stress-assisted discontinuous grain growth and its effect on the deformation behavior of nanocrystalline aluminum thin films, Acta Mater. 54 (8) (2006) 2253–2263.
- [17] A. Rajabzadeh, F. Mompiou, S. Lartigue-Korinek, N. Combe, M. Legros, D.A. Molodov, The role of disconnections in deformation-coupled grain boundary migration, Acta Mater. 77 (2014) 223–235.
- [18] O. Renk, A. Hohenwarter, R. Pippan, Cyclic deformation behavior of a 316L austenitic stainless steel processed by high pressure torsion, Adv. Eng. Mater. 14 (11) (2012) 948–954.
- [19] R.Z. Valiev, T.G. Langdon, Principles of equal-channel angular pressing as a processing tool for grain refinement, Prog. Mater. Sci. 51 (7) (2006) 881–981.
- [20] P.G. Sanders, J.A. Eastman, J.R. Weertman, Elastic and tensile behavior of nanocrystalline copper and palladium, Acta Mater. 45 (10) (1997) 4019–4025.
- [21] A.J. Detor, C.A. Schuh, Tailoring and patterning the grain size of nanocrystalline alloys, Acta Mater. 55 (1) (2007) 371–379.
- [22] M.R. He, P.J. Felfer, S. Dasgupta, S.K. Samudrala, P.J. Malone, G. Feng, D.S. Gianola, Understanding the mechanical behavior of nanocrystalline Al–O thin films with complex microstructures, Acta Mater. 77 (2014) 269–283.
- [23] B. Oberdorfer, D. Setman, E.M. Steyskal, A. Hohenwarter, W. Sprengel, M. Zehetbauer, R. Würschum, Grain boundary excess volume and defect annealing of copper after high-pressure torsion, Acta Mater. 68 (2014) 189–195.
- [24] T.J. Rupert, J.R. Trelewicz, C.A. Schuh, Grain boundary relaxation strengthening of nanocrystalline Ni–W alloys, J. Mater. Res. 27 (9) (2012) 1285–1294.
- [25] T.J. Rupert, C.A. Schuh, Mechanically driven grain boundary relaxation: a mechanism for cyclic hardening in nanocrystalline Ni, Phil. Mag. Lett. 92 (1) (2012) 20–28.
- [26] J. Weissmüller, Alloy effects in nanostructures, Nanostruct. Mater. 3 (1–6) (1993) 261–272.
- [27] T. Frolov, D.L. Olmsted, M. Asta, Y. Mishin, Structural phase transformations in metallic grain boundaries, Nat. Commun. 4 (2013) 1899.
- [28] T.G. Nieh, J. Wadsworth, Hall-Petch relation in nanocrystalline solids, Scripta Metall. Mater. 25 (4) (1991) 955–958.
- [29] A.C. Lund, C.A. Schuh, Strength asymmetry in nanocrystalline metals under multiaxial loading, Acta Mater. 53 (11) (2005) 3193–3205.
- [30] H. Van Swygenhoven, M. Spaczer, A. Caro, D. Farkas, Competing plastic deformation mechanisms in nanophase metals, Phys. Rev. B 60 (1) (1999) 22.
- [31] J. Schiøtz, T. Vegge, F.D. Di Tolla, K.W. Jacobsen, Atomic-scale simulations of the mechanical deformation of nanocrystalline metals, Phys. Rev. B 60 (17) (1999) 11971.
- [32] A. Khalajhedayati, T.J. Rupert, Emergence of localized plasticity and failure through shear banding during microcompression of a nanocrystalline alloy, Acta Mater. 65 (2014) 326–337.
- [33] H. Zhang, D.J. Srolovitz, J.F. Douglas, J.A. Warren, Grain boundaries exhibit the dynamics of glass-forming liquids, Proc. Natl. Acad. Sci. Unit. States Am. 106 (19) (2009) 7735–7740.
- [34] G. Kumar, D. Rector, R.D. Conner, J. Schroers, Embrittlement of Zr-based bulk metallic glasses, Acta Mater. 57 (12) (2009) 3572–3583.
- [35] H.B. Ke, P. Wen, H.L. Peng, W.H. Wang, A.L. Greer, Homogeneous deformation of metallic glass at room temperature reveals large dilatation, Scripta Mater. 64 (10) (2011) 966–969.
- [36] D.J. Magagnosc, G. Feng, L. Yu, X. Cheng, D.S. Gianola, Isochemical control over structural state and mechanical properties in Pd-based metallic glass by sputter deposition at elevated temperatures, Apl. Mater. 4 (8) (2016), 086104.
- [37] D.J. Magagnosc, G. Kumar, J. Schroers, P. Felfer, J.M. Cairney, D.S. Gianola, Effect of ion irradiation on tensile ductility, strength and fictive temperature in metallic glass nanowires, Acta Mater. 74 (2014) 165–182.

- [38] M. Utz, P.G. Debenedetti, F.H. Stillinger, Atomistic simulation of aging and rejuvenation in glasses, Phys. Rev. Lett. 84 (7) (2000) 1471.
- [39] C.E. Packard, E.R. Homer, N. Al-Aqeeli, C.A. Schuh, Cyclic hardening of metallic glasses under Hertzian contacts: experiments and STZ dynamics simulations, Phil. Mag. 90 (10) (2010) 1373–1390.
- [40] W. Dmowski, Y. Yokoyama, A. Chuang, Y. Ren, M. Umemoto, K. Tsuchiya, A. Inoue, T. Egami, Structural rejuvenation in a bulk metallic glass induced by severe plastic deformation, Acta Mater. 58 (2) (2010) 429–438.
- [41] S.V. Ketov, Y.H. Sun, S. Nachum, Z. Lu, A. Checchi, A.R. Beraldin, H.Y. Bai, W.H. Wang, D.V. Louzguine-Luzgin, M.A. Carpenter, A.L. Greer, Rejuvenation of metallic glasses by non-affine thermal strain, Nature 524 (7564) (2015) 200.
- [42] Y. Sun, A. Concustell, A.L. Greer, Thermomechanical processing of metallic glasses: extending the range of the glassy state, Nature Reviews Materials 1 (2016) 16039.
- [43] A. Peterlongo, A. Miotello, R. Kelly, Laser-pulse sputtering of aluminum: vaporization, boiling, superheating, and gas-dynamic effects, Phys. Rev. 50 (6) (1994) 4716.
- [44] M. Sorescu, E.T. Knobbe, Induced anisotropy and phase transformation in metallic glasses by pulsed-excimer-laser irradiation, Phys. Rev. B 49 (5) (1994) 3253.
- [45] C.J. Lin, F. Spaepen, Nickel-niobium alloys obtained by picosecond pulsed laser quenching, Acta Metall. 34 (7) (1986) 1367–1375.
- [46] B. Rethfeld, K. Sokolowski-Tinten, D. Von Der Linde, S.I. Anisimov, Timescales in the response of materials to femtosecond laser excitation, Appl. Phys. Mater. Sci. Process 79 (4) (2004) 767–769.
- [47] M.V. Shugaev, C. Wu, O. Armbruster, A. Naghilou, N. Brouwer, D.S. Ivanov, T.J.-Y. Derrien, N.M. Bulgakova, W. Kautek, B. Rethfeld, L.V. Zhigilei, Fundamentals of ultrafast laser-material interaction, MRS Bull. 41 (12) (2016) 960–968
- [48] M.P. Echlin, A. Mottura, C.J. Torbet, T.M. Pollock, A new TriBeam system for three-dimensional multimodal materials analysis, Rev. Sci. Instrum. 83 (2) (2012), 023701.
- [49] M.P. Echlin, M. Straw, S. Randolph, J. Filevich, T.M. Pollock, The TriBeam system: femtosecond laser ablation in situ SEM, Mater. Char. 100 (2015) 1–12.
- [50] K. Furusawa, K. Takahashi, H. Kumagai, K. Midorikawa, M. Obara, Ablation characteristics of Au, Ag, and Cu metals using a femtosecond Ti: sapphire laser, Appl. Phys. A 69 (1) (1999) S359–S366.
- [51] V.V. Zhakhovsky, K.P. Migdal, N.A. Inogamov, S.I. Anisimov, MD simulation of steady shock-wave fronts with phase transition in single-crystal iron, In: AIP Conference Proceedings, vol. 1793, AIP Publishing, 2017, January, No. 1, p. 070003
- [52] S.I. Ashitkov, V.V. Zhakhovsky, N.A. Inogamov, P.S. Komarov, M.B. Agranat, G.I. Kanel, the behavior of iron under ultrafast shock loading driven by a femtosecond laser, In: AIP Conference Proceedings, vol. 1793, AIP Publishing, 2017, January, No. 1, p. 100035.
- [53] B.J. Demaske, V.V. Zhakhovsky, N.A. Inogamov, I.I. Oleynik, Ultrashort shock waves in nickel induced by femtosecond laser pulses, Phys. Rev. B 87 (5) (2013), 054109.
- [54] C. Wu, M.S. Christensen, J.M. Savolainen, P. Balling, L.V. Zhigilei, Generation of subsurface voids and a nanocrystalline surface layer in femtosecond laser irradiation of a single-crystal Ag target, Phys. Rev. B 91 (3) (2015), 035413.
- [55] M. Gill-Comeau, L.J. Lewis, Ultrashort-pulse laser ablation of nanocrystalline aluminum, Phys. Rev. B 84 (22) (2011), 224110.
- [56] S. Marinier, L.J. Lewis, Femtosecond laser ablation of Cu_x Zr_{1-x} bulk metallic glasses: a molecular dynamics study, Phys. Rev. B 92 (18) (2015), 184108.
- [57] A. Khalajhedayati, Z. Pan, T.J. Rupert, Manipulating the interfacial structure of nanomaterials to achieve a unique combination of strength and ductility, Nat. Commun. 7 (2016), 10802.
- [58] A. Khalajhedayati, T.J. Rupert, High-temperature stability and grain boundary complexion formation in a nanocrystalline Cu-Zr alloy, JOM (J. Occup. Med.) 67 (12) (2015) 2788–2801.
- [59] J.M. Liu, Simple technique for measurements of pulsed Gaussian-beam spot sizes, Optic Lett. 7 (5) (1982) 196–198.
- [60] J. Bonse, S. Baudach, J. Krüger, W. Kautek, M. Lenzner, Femtosecond laser ablation of silicon–modification thresholds and morphology, Appl. Phys. A 74 (1) (2002) 19–25.
- [61] W.C. Oliver, G.M. Pharr, Measurement of hardness and elastic modulus by instrumented indentation: advances in understanding and refinements to methodology, J. Mater. Res. 19 (1) (2004) 3–20.
- [62] R. Saha, W.D. Nix, Effects of the substrate on the determination of thin film mechanical properties by nanoindentation, Acta Mater. 50 (1) (2002) 23–38.
- [63] P.G. Callahan, J.C. Stinville, E.R. Yao, M.P. Echlin, M.S. Titus, M. De Graef, D.S. Gianola, T.M. Pollock, Transmission scanning electron microscopy: defect observations and image simulations, Ultramicroscopy 186 (2018) 49–61.
- [64] S. Amoruso, R. Bruzzese, M. Vitiello, N.N. Nedialkov, P.A. Atanasov, Experimental and theoretical investigations of femtosecond laser ablation of aluminum in vacuum, J. Appl. Phys. 98 (4) (2005), 044907.
- [65] A.D. Rakić, Algorithm for the determination of intrinsic optical constants of metal films: application to aluminum, Appl. Optic. 34 (22) (1995) 4755–4767.

- [66] P.B. Johnson, R.W. Christy, Optical constants of the noble metals, Phys. Rev. B 6 (12) (1972) 4370.
- [67] Marvin R. Querry, Optical Constants of Minerals and Other Materials from the Millimeter to the Ultraviolet, U.S. Army Armament Munitions Chemical Command Chemical Research, Development & Engineering Center, 1987.
- [68] J. Sommer, C. Herzig, Direct determination of grain-boundary and dislocation self-diffusion coefficients in silver from experiments in type-C kinetics, J. Appl. Phys. 72 (7) (1992) 2758–2766.
- [69] B. Fultz, H.N. Frase, Grain boundaries of nanocrystalline materials—their widths, compositions, and internal structures, Hyperfine Interact. 130 (1–4) (2000) 81–108.
- [70] J.R. Trelewicz, C.A. Schuh, Grain boundary segregation and thermodynamically stable binary nanocrystalline alloys, Phys. Rev. B 79 (9) (2009), 094112.
- [71] K. Durst, B. Backes, M. Göken, Indentation size effect in metallic materials: correcting for the size of the plastic zone, Scripta Mater. 52 (11) (2005) 1093–1097.
- [72] M.R. He, S.K. Samudrala, G. Kim, P.J. Felfer, A.J. Breen, J.M. Cairney, D.S. Gianola, Linking stress-driven microstructural evolution in nanocrystalline aluminium with grain boundary doping of oxygen, Nat. Commun. 7 (2016), 11225.
- [73] F. Tang, D.S. Gianola, M.P. Moody, K.J. Hemker, J.M. Cairney, Observations of grain boundary impurities in nanocrystalline Al and their influence on microstructural stability and mechanical behaviour, Acta Mater. 60 (3) (2012) 1038–1047
- [74] M. Iyer, V. Gavini, T.M. Pollock, Energetics and nucleation of point defects in aluminum under extreme tensile hydrostatic stresses, Phys. Rev. B 89 (1) (2014), 014108
- [75] T.Y. Tsui, W.C. Oliver, G.M. Pharr, Influences of stress on the measurement of mechanical properties using nanoindentation: Part I. Experimental studies in an aluminum alloy, J. Mater. Res. 11 (3) (1996) 752–759.
- [76] L.V. Zhigilei, Z. Lin, D.S. Ivanov, Atomistic modeling of short pulse laser ablation of metals: connections between melting, spallation, and phase explosion, J. Phys. Chem. C 113 (27) (2009) 11892–11906.
- [77] A.Y. Vorobyev, V.M. Kuzmichev, N.G. Kokody, P. Kohns, J. Dai, C. Guo, Residual thermal effects in Al following single ns-and fs-laser pulse ablation, Appl. Phys. Mater. Sci. Process 82 (2) (2006) 357–362.
- [78] A.Y. Vorobyev, C. Guo, Direct observation of enhanced residual thermal energy coupling to solids in femtosecond laser ablation, Appl. Phys. Lett. 86 (1) (2005), 011916.
- [79] E.O. Hall, The deformation and ageing of mild steel: III discussion of results, Proc. Phys. Soc. B 64 (9) (1951) 747.
- [80] D. Tabor, The hardness and strength of metals, J. Inst. Met. 79 (1) (1951) 1–18.
- [81] J.W. Wyrzykowski, M.W. Grabski, The Hall–Petch relation in aluminium and its dependence on the grain boundary structure, Philos. Mag. A 53 (4) (1986) 505, 520

- [82] M.A. Atwater, H. Bahmanpour, R.O. Scattergood, C.C. Koch, The thermal stability of nanocrystalline cartridge brass and the effect of zirconium additions, J. Mater. Sci. 48 (1) (2013) 220–226.
- [83] Z.W. Wang, Z.Y. Li, S.J. Park, A. Abdela, D. Tang, R.E. Palmer, Quantitative Z-contrast imaging in the scanning transmission electron microscope with size-selected clusters, Phys. Rev. B 84 (7) (2011), 073408.
- [84] Y. Oishi, W.D. Kingery, Self-diffusion of oxygen in single crystal and polycrystalline aluminum oxide, J. Chem. Phys. 33 (2) (1960) 480–486.
- [85] M.J. Demkowicz, A.S. Argon, Liquidlike atomic environments act as plasticity carriers in amorphous silicon, Phys. Rev. B 72 (24) (2005), 245205.
- [86] J.L. Hostetler, A.N. Smith, D.M. Czajkowsky, P.M. Norris, Measurement of the electron-phonon coupling factor dependence on film thickness and grain size in Au, Cr, and Al, Appl. Optic. 38 (16) (1999) 3614–3620.
- [87] H.E. Elsayed-Ali, T. Juhasz, G.O. Smith, W.E. Bron, Femtosecond thermoreflectivity and thermotransmissivity of polycrystalline and single-crystalline gold films, Phys. Rev. B 43 (5) (1991) 4488.
- [88] C.A. Volkert, A. Donohue, F. Spaepen, Effect of sample size on deformation in amorphous metals, J. Appl. Phys. 103 (8) (2008), 083539.
- [89] M. Tang, W.C. Carter, R.M. Cannon, Grain boundary transitions in binary alloys, Phys. Rev. Lett. 97 (7) (2006), 075502.
- [90] A. Rajabzadeh, F. Mompiou, S. Lartigue-Korinek, N. Combe, M. Legros, D.A. Molodov, The role of disconnections in deformation-coupled grain boundary migration. Acta Mater. 77 (2014) 223–235.
- [91] A.C. Lund, C.A. Schuh, Strength asymmetry in nanocrystalline metals under multiaxial loading, Acta Mater. 53 (11) (2005) 3193–3205.
- [92] A.C. Lund, T.G. Nieh, C.A. Schuh, Tension/compression strength asymmetry in a simulated nanocrystalline metal, Phys. Rev. B 69 (1) (2004), 012101.
- [93] L. Zhang, C. Lu, Y. Shibuta, Shear response of grain boundaries with metastable structures by molecular dynamics simulations, Model. Simulat. Mater. Sci. Eng. 26 (3) (2018), 035008.
- [94] T.J. Rupert, Strain localization in a nanocrystalline metal: atomic mechanisms and the effect of testing conditions, J. Appl. Phys. 114 (3) (2013), 033527.
- [95] E.D. Cubuk, R.J.S. Ivancic, S.S. Schoenholz, D.J. Strickland, A. Basu, Z.S. Davidson, J. Fontaine, J.L. Hor, Y.-R. Huang, Y. Jiang, Y. Jiang, Y. Jiang, N.C. Keim, K.D. Koshigan, J.A. Lefever, T. Liu, X.-G. Ma, D.J. Magagnosc, E. Morrow, C.P. Ortiz, J.M. Rieser, A. Shavit, T. Still, Y. Xu, Y. Zhang, K.N. Nordstrom, P.E. Arratia, R.W. Carpick, D.J. Durian, Z. Fakhraai, D.J. Jerolmack, D. Lee, J. Li, R. Riggleman, K.T. Turner, A.G. Yodh, D.S. Gianola, A.J. Liu, Structure-property relationships from universal signatures of plasticity in disordered solids, Science 358 (6366) (2017) 1033–1037.